

Preempting Fermion Sign Problem: Unveiling Quantum Criticality through Nonequilibrium Dynamics

Yin-Kai Yu,^{1,2,3} Zhi-Xuan Li,¹ Shuai Yin,^{1,*} and Zi-Xiang Li^{2,3,†}

¹*Guangdong Provincial Key Laboratory of Magnetoelectric Physics and Devices, School of Physics, Sun Yat-sen University, Guangzhou 510275, China*

²*Beijing National Laboratory for Condensed Matter Physics & Institute of Physics, Chinese Academy of Sciences, Beijing 100190, China*

³*University of Chinese Academy of Sciences, Beijing 100049, China*

(Dated: October 25, 2024)

The notorious fermion sign problem, arising from fermion statistics, constitutes one of the main obstacles of deciphering quantum many-body systems by numerical approach. The progress in overcoming sign problem will definitely lead to a great leap in various areas of modern physics. Here, by deviating from the conventional cognition that nonequilibrium studies should be more complicated than equilibrium cases, we propose an innovative framework based on nonequilibrium critical dynamics to preempt sign problem and investigate quantum critical point in fermionic model through numerically exact quantum Monte Carlo (QMC) simulation. By virtue of universal scaling theory of imaginary-time relaxation dynamics, we demonstrate that accurate critical point and critical exponents can be obtained in the short-time stage, in which the sign problem is not severe such that the QMC is accessible. After confirming the effectiveness of the method in two typical interacting fermionic models featuring Dirac quantum critical point (QCP), we for the first time reveal the quantum phase diagram in the Hubbard model hosting SU(3)-symmetric Dirac fermions, and find that the QCP between Dirac semi-metal and a λ_8 -antiferromagnetic phase belongs to a new universality class different from the previously known Gross-Neveu transitions.

Introduction — The sign structure of the quantum many-body wave functions works like a double-edged sword. On the one hand, it endows fertile exotic phenomena ranging from condensed matter physics [1, 2] to high energy physics [3]. Quantum Monte-Carlo (QMC) is among the most important theoretical approaches to study the exotic properties of strongly correlated quantum many-body systems [4–6], because it is intrinsically unbiased and numerically exact. However, on the other hand, the sign structure in the wave function results in the notorious sign problem [7–11], which considerably plagues the application of QMC to investigating interacting models potentially featuring intriguing physics, for instance, the Hubbard model at generic filling [12, 13] and the lattice QCD at finite baryon density [14]. Since the general solution of sign problem is lacking and non-deterministic polynomial (NP)-hard [9], establishing novel generic strategies to attack the sign problem in QMC will definitely provoke significant advances in the realm of quantum many-body physics [15–36].

Among various exotic phenomena in quantum many-body systems, quantum criticality emerges as a particularly crucial and fascinating one. The underlying physics of the quantum critical point (QCP) lays the foundation for achieving a unified theoretical framework to characterize different phases and phase transitions [37–41]. Moreover, quantum criticality is intimately associated with fundamentally important phenomena in condensed matter physics such as high- T_c superconductivity [42–

44] and strange metallicity [45, 46]. The understanding of QCP in a non-perturbative way is severely hindered by the sign problem likewise. Developing a generic unbiased theoretical approach to decipher quantum criticality not only has overarching meaning in fundamental theory, but also immensely promotes the research on the exotic phenomena emerging in quantum materials.

Here, we propose a general framework to preempt sign problem in QMC and unveil the quantum criticality. Generally, fathoming the nonequilibrium properties in quantum many-body systems is substantially challenging, compared with the equilibrium ones. However, we leverage the nonequilibrium behavior and demonstrate that the short-time critical dynamics, which was first proposed in classical systems [47] and used to detect the classical critical behaviors [48] and then generalized to imaginary-time dynamics of QCP [49], provides an ingenious strategy to reliably probe quantum criticality in the presence of sign problem, as illustrated in Fig. 1a. The underling mechanism is that in the short-time stage of imaginary-time relaxation for some typical initial states, (1) universal scaling behaviors manifesting the quantum criticality appear [49, 50]; (2) the sign problem remains mild in this stage such that the reliable results are accessible by QMC simulation. Hence, bestowing the scaling of short-time dynamics [47–50], we can accurately determine critical properties of the QCP, while the sign problem therein, whose severity generally exponentially increases with the imaginary time [9, 51], is largely alleviated compared with the equilibrium one involving long imaginary-time evolution.

In the following, we demonstrate the framework by studying two typical interacting fermionic models fea-

* yinsh6@mail.sysu.edu.cn

† zixiangli@iphy.ac.cn

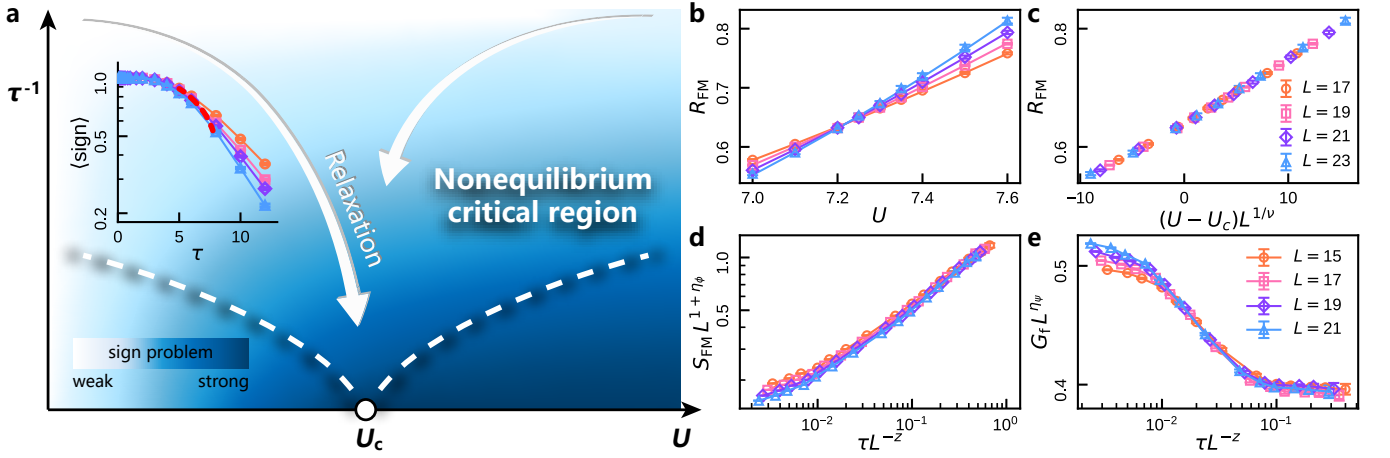


FIG. 1. **Scheme of preempting sign problem to probe quantum criticality via short-time critical dynamics and the application in single-Dirac-fermion Hubbard model.** **a**, With some typical initial states, scaling behaviors governed by the QCP are reflected in the short-time stage, in which the sign problem is still weak as shown in the inset. The red dashed line therein marks the average sign at $\tau = 0.3L^z$. **b**, Determination of QCP as $U_c = 7.220(37)$ via the intersection points of curves of the correlation length ratio R_{FM} versus U for different sizes at $\tau = 0.3L^z$ with DSM initial state. **c**, Determination of $1/\nu = 1.18(3)$ by scaling collapse of R_{FM} versus rescaled $(U - U_c)L^{1/\nu}$. **d**, Determination of $\eta_\phi = 0.33(2)$ via scaling collapse of curves of the structure factor S_{FM} versus rescaled τ at U_c . **e**, Determination of $\eta_\psi = 0.135(2)$ via scaling collapse of curves of the fermion correlation G_f versus rescaled τ at U_c .

turing Dirac QCP. We unambiguously show that accurate critical properties are accessed through short-time dynamics, despite the presence of sign problem. More remarkably, we adopt the approach to investigate a paradigmatic strongly interacting model hosting Dirac fermions with SU(3) symmetry, namely the SU(3) staggered-flux Hubbard model, which is sign problematic in any known algorithm. For the first time we unravel the ground-state phase diagram of the model and reveal the critical properties of the quantum phase transition between the Dirac semi-metal (DSM) and a λ_8 -antiferromagnetic (AFM) phase. Intriguingly, the QCP belongs to a novel universality class distinct from previous Gross-Neveu transitions.

Theoretical framework — We consider the imaginary-time relaxation dynamics for which the wave function $|\psi(\tau)\rangle$ evolves according to the imaginary-time Schrödinger equation $-\frac{\partial}{\partial\tau}|\psi(\tau)\rangle = H|\psi(\tau)\rangle$ imposed by the normalization condition. As its long-time solution is the ground state, this equation provides a routine method to access ground-state properties in numerical computations [51]. Moreover, near the QCP, it was shown that universal scaling behaviors manifest themselves not only at the ground state, but also in the imaginary-time relaxation process. Particularly, with initial states corresponding to the fixed points of scale transformation, the short-time dynamics of observable O satisfies the following scaling form [49, 50]:

$$O(\tau, g, L) = L^{-\kappa} f_O(gL^{\frac{1}{\nu}}, \tau L^{-z}), \quad (1)$$

where L is linear system size and g is the distance to the critical point, κ is the scaling dimension of O , and ν is the correlation-length exponent, z is dynamical exponent

which is generally one in Dirac QCP. Note that all critical exponents in Eq. (1) are controlled by the QCP in the ground state. Accordingly, from Eq. (1), one can achieve critical properties from the expectation value of O in the relaxation process. This nonequilibrium approach is notably different from the conventional one which requires that the ground state should be determined through the evolution of long imaginary time. Because in general the severity of sign problem exponentially increases with τ in QMC [9], the sign problem in short-time stage of relaxation is significantly mitigated compared with the simulation on ground-state properties, thereby enabling the large-scale QMC simulation with high accuracy despite the presence of sign problem. In the following, we elucidate the theoretical framework by systematically studying several representative models with sign problem.

Single-Dirac-fermion Hubbard model — We first consider the SLAC fermion Hubbard model with the Hamiltonian [52–54]:

$$H = \sum_{i, \mathbf{R}} t_{\mathbf{R}} c_{i\uparrow}^\dagger c_{i+\mathbf{R}\downarrow} + \text{h.c.} + U \sum_i \left(n_{i\uparrow} - \frac{1}{2} \right) \left(n_{i\downarrow} - \frac{1}{2} \right), \quad (2)$$

where $t_{\mathbf{R}} = \frac{i(-1)^{R_x}}{L} \sin \pi \frac{R_x}{L} \delta_{R_y,0} + \frac{(-1)^{R_y}}{L} \sin \pi \frac{R_y}{L} \delta_{R_x,0}$ is the amplitude of long-range hopping and U is the strength of repulsive interaction. The model is sign problematic in any known QMC algorithm. Nonetheless, since the sign problem is relatively benign, previous QMC study reveals a chiral Ising QCP separating Dirac semimetal (DSM) phase and ferromagnetic (FM) phase [52].

Here, we present the procedure for unraveling the crit-

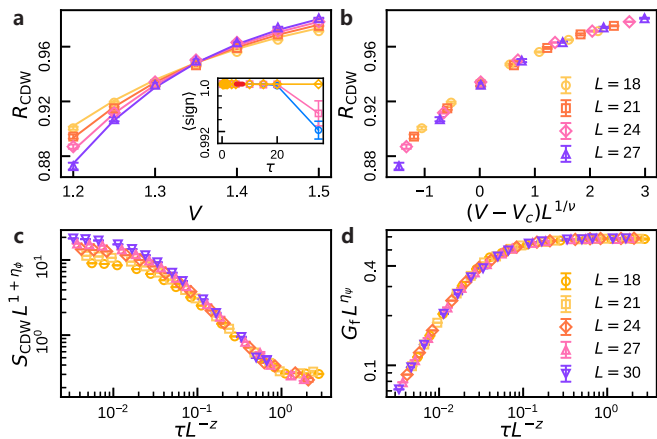


FIG. 2. **Probing quantum criticality via short-time critical dynamics in spinless t - V model with CDW initial state.** **a**, Determination of QCP as $V_c = 1.35(1)$ via the intersection points of R_{CDW} versus V for different L at $\tau = 0.3L^z$. Shown in Inset is the evolution of average sign with red dashed curve marks $\tau = 0.3L^z$. **b**, Determination of $1/\nu = 1.30(18)$ via scaling collapse of R_{CDW} versus rescaled $(V - V_c)L^{1/\nu}$. **c-d**, Determination of $\eta_\phi = 0.49(5)$ and $\eta_\psi = 0.073(4)$ via scaling collapse of short-time dynamics of S_{CDW} and G_f versus rescaled τ , respectively.

ical properties via the short-time scaling of the observable as dictated in Eq. (1). In the conventional projector QMC approach, a sufficiently long evolution time should be implemented to ensure that the ground-state properties are accessed, resulting in the severe sign problem exponentially increasing with τ , as shown in Fig. 1. We overcome this critical difficulty owing to the short-time critical relaxation dynamics. To determine the critical point via Eq. (1), we consider observable O as the dimensionless correlation length ratio R_{FM} for the FM order (See SM Sec. II for the detailed definition [55]) and fix τ at short-time stage as $\tau = 0.3L^z$, where $z = 1$ due to the nature of Dirac QCP. Accordingly, R_{FM} satisfies $R_{\text{FM}} = f_R(gL^{1/\nu})$ where $g = U - U_c$. We show the numerical results in Fig. 1b, in which the crossing point of R_{FM} versus U for different L reveals a quantum phase transition from DSM to FM phase occurring at $U_c = 7.220(37)$. Furthermore, we perform data collapse analysis of R_{FM} for different L versus $(U - U_c)L^{1/\nu}$ and achieve accurate critical exponent $1/\nu = 1.18(3)$, as shown in Fig. 1c. Furthermore, fixing $U = U_c$, we calculate the imaginary-time evolution of FM structure order S_{FM} and fermion correlation G_f (defined in SM Sec. II [55]), whose scaling dimensions are $(1 + \eta_\phi)$ and η_ψ , respectively [50, 52]. By making the rescaled curves of $S_{\text{FM}}L^{(1+\eta_\phi)}$ and $G_fL^{\eta_\psi}$ versus τL^{-z} for different L collapse according to Eq. (1) as shown in Figs. 1d and 1e, we achieve the anomalous dimensions of the order parameter boson $\eta_\phi = 0.33(2)$ and the Dirac fermion $\eta_\psi = 0.135(2)$, respectively.

Comparing the critical point and critical exponents

evaluated here with previous results, we find that all are approximately consistent with previous study of Gutzwiller QMC [52] and functional renormalization group [56]. Notice that since sign problem is largely alleviated in our work owing to the short evolution time, we can achieve larger system size $L = 23$ [55], compared with previous studies, and thus reach the reliable results of critical exponents. Consequently, we unambiguously demonstrate that the short-time dynamics via QMC simulation provides a powerful approach to fathom quantum critical properties in sign-problematic strongly interacting models.

Spinless t - V model — To further demonstrate the framework of our approach, we study another typical interacting Dirac-fermion model, termed as Honeycomb spinless t - V model, with the Hamiltonian: [17, 57–59]:

$$H = -t \sum_{\langle ij \rangle} c_i^\dagger c_j + V \sum_{\langle ij \rangle} \left(n_i - \frac{1}{2} \right) \left(n_j - \frac{1}{2} \right), \quad (3)$$

where t is nearest-neighbor (NN) hopping amplitude and V denotes the strength of NN density interaction. The appearance of sign problem in Eq. (3) depends on the channel of Hubbard-Strotonovich (H-S) transformation. Hence, the model provides a genuine platform to confirm the accuracy and feasibility of our approach to unravel QCP in the presence of sign problem. Previous sign-free QMC studies, with the H-S transformation in the hopping channel, reveal the critical properties of the QCP separating DSM and charge-density-wave (CDW) phases [58]. Here, we decouple the interaction in the sign-problematic density channel and study the QCP via short-time relaxation dynamics [60].

The procedure is the same as the previous section, except that the initial state is chosen as the CDW fully ordered state. We will demonstrate that the initial state can be flexibly selected in our approach, thereby offering various routes to extract critical properties. We fix $\tau = 0.3L^z$, and determine QCP from the crossing point of curves of correlation-length ratio R_{CDW} versus V (R_{CDW} is defined in SM Sec. III [55]), as displayed in Fig. 2a, giving rise to $V_c = 1.35(1)$. The scaling collapse analysis determines the value of ν as $1/\nu = 1.30(18)$. Additionally, the anomalous dimensions $\eta_\phi = 0.49(5)$ and $\eta_\psi = 0.073(4)$ are obtained from the evolution of the CDW structure factor S_{CDW} and the fermion correlation G_f (defined in SM Sec. III [55]), respectively, at V_c . Both V_c and η_ϕ are consistent with previous numerical results, while η_ψ , to the best of our knowledge, is numerically determined for the first time, and is consistent with the previous results of the functional renormalization group [56]. The similar computation with DSM initial state yields the consistent results, with the details included in the SM [55]. Hence, these results for model (3) further establish the feasibility of the approach based on short-time dynamics in accessing the critical properties in the presence of sign problem. Moreover, the flexible choice of initial states provide benchmarks for the results,

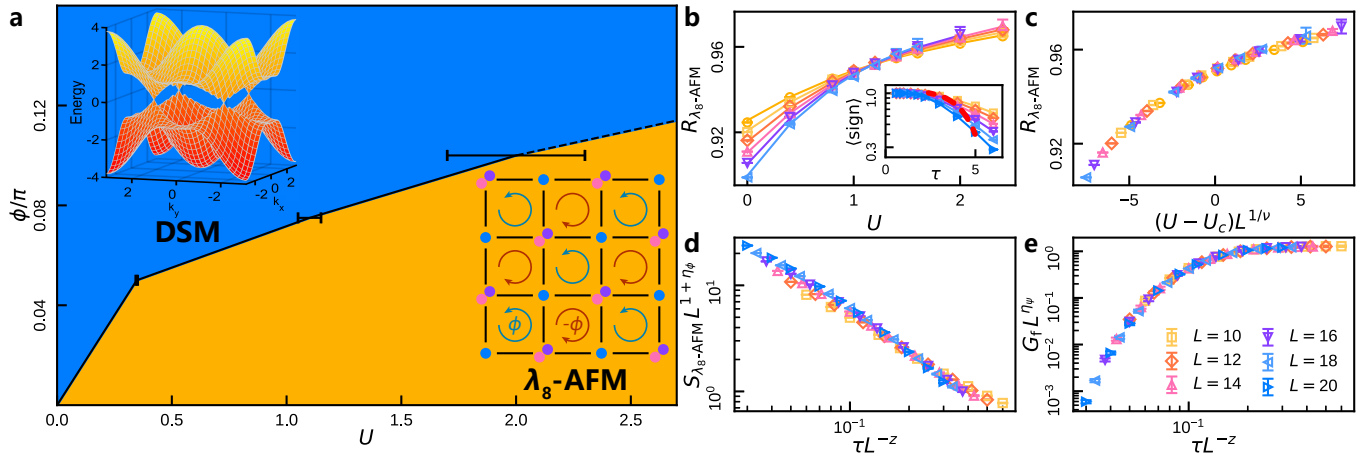


FIG. 3. **Phase diagram and quantum criticality in SU(3) Hubbard model detected by short-time dynamics with λ_8 -AFM initial state.** **a**, Phase diagram determined via short-time dynamics. Insets show the energy spectra of DSM state (upper left) and Sketch of λ_8 -AFM order in which a fermion with one flavor (blue) is situated at one sublattice and double fermions with the other two flavors (pink and violet) are situated at the other sublattice (lower right). **b-c**, Critical point $U_c = 1.10(5)$ for $\phi = 0.075\pi$ and $1/\nu = 0.68(5)$ determined via curves of $R_{\lambda_8\text{-AFM}}$ versus U for different L at $\tau = 0.25L^z$. Shown in Inset of **b** is the evolution of average sign with red dashed curve marks $\tau = 0.25L^z$. **d-e**, $\eta_\phi = 0.55(5)$ and $\eta_\psi = 0.15(3)$ determined via the scaling collapse of evolution curves of $S_{\lambda_8\text{-AFM}}$ and G_f , respectively.

further improving the accuracy of the approach.

SU(3) Hubbard model — The successful application of the method in previous two models encourages us to study the critical properties in unexplored models. In the following, we implement the approach to systematically investigate a sign-problematic interacting model featuring exotic Dirac QCP belonging to a novel universality class. We consider SU(3) Hubbard model with staggered magnetic flux on square lattice, described by the following Hamiltonian:

$$H = - \sum_{\langle ij \rangle \alpha} t_{ij} c_{i\alpha}^\dagger c_{j\alpha} + \frac{U}{2} \sum_i \left(\sum_\alpha n_{i\alpha} - \frac{3}{2} \right)^2, \quad (4)$$

where $\alpha = 1, 2, 3$ is the flavor index of fermion, U is repulsive Hubbard interaction strength, and $t_{ij} = te^{i\theta_{ij}}$, in which $t = 1$ is set as energy unit. As illustrated in Fig. 3a, the magnetic flux in each plaquette is $\sum_{\square} \theta_{ij} = (-1)^{i_x+i_y} \phi$. For non-zero ϕ , the energy dispersion of Eq. (4) in the non-interacting limit features two Dirac points located at momenta $(\pm \frac{\pi}{2}, \pm \frac{\pi}{2})$, as shown in SM [55]. We fix our simulation at half filling such that the Fermi level is located at Dirac points. The model of Eq. (2) respects $SU(3) \times Z_2$ symmetry, where $SU(3)$ is the rotation symmetry in flavor space and Z_2 is the sublattice symmetry which exchanges the two sublattices on the staggered-flux square lattice with each unit cell containing two sites.

The $SU(N)$ symmetry plays overarching roles in modern physics. For instance, the $SU(3)$ symmetry lays the foundation for strong interaction between quarks [3]. Recently, fermionic interacting models with $SU(N)$ symmetry have been realized in optical lattice [61, 62]. Extensive theoretical and numerical efforts, including sign-free

QMC simulation, are devoted to understanding the exotic phenomena arising from the interplay between strong interaction, Dirac fermions and multi-flavor physics [63–67]. However, despite its fundamental importance, the unbiased numerical study on $SU(N)$ -symmetric model with repulsive Hubbard interaction for odd N is scarce, largely due to the presence of notorious sign problem in QMC simulation. Hence, we implement our approach to preempt sign problem and unravel the quantum phases and exotic QCP in Eq. (4), which is a minimal interacting model featuring $SU(N)$ symmetry with odd N .

Before embarking on QMC simulation, we perform a mean-field calculation to detect the feature of the ground state schematically. The mean-field calculation shows that an antiferromagnetic (AFM) order is favored by the strong Hubbard interaction [55]. The order parameter is characterized in terms of the generators of $SU(3)$ symmetry group, which is expressed by the eight Gell-Mann matrices in flavor space for convenience [68] (The details of the $SU(3)$ algebra are introduced in SM [55]). In stark contrast to the case of $SU(2)$, only one Gell-Mann matrix is full-rank without zero eigenvalue, dubbed as $\lambda_8 = \text{diag}(\frac{1}{\sqrt{3}}, \frac{1}{\sqrt{3}}, -\frac{2}{\sqrt{3}})$. Consequently, for the AFM order in $SU(3)$ fermions, only the order parameter associated with λ_8 is the mass term fully opening spectral gap in Dirac fermions, which is expressed as $m_{\lambda_8\text{-AFM}} = \frac{1}{L^2} \sum_{i,\alpha,\beta} c_{i\alpha}^\dagger \lambda_8^{\alpha\beta} c_{i\beta} (-1)^{i_x+i_y}$. The mean-field calculation also confirms that such AFM order is energetically favorable in model Eq. (4) [55].

In the λ_8 -AFM ordered phase, the Z_2 sublattice symmetry is broken and the $SU(3)$ symmetry is broken into $SU(2) \times U(1)$ (See SM Sec. IV for details [55]), as illustrated in Fig. 3a. Accordingly, the order parameter man-

ifold is $\frac{SU(3) \times Z_2}{SU(2) \times U(1)}$, which is remarkably different from the universality classes of the Gross-Neveu QCP studied previously. Thus, the QCP separating DSM and λ_8 -AFM phase is a novel Dirac QCP.

To reveal the critical properties, we perform short-time QMC simulation with fully ordered initial state by fixing $\phi = 0.075\pi$ and $\tau L^{-z} = 0.25$ where $z = 1$. The results of correlation length ratio $R_{\lambda_8\text{-AFM}}$ for λ_8 -AFM order (defined in SM Sec. IV [55]) are shown in Fig. 3b and the crossing points dictate the phase transition point from DSM to λ_8 -AFM phase occurring at $U_c = 1.10(5)$. We also compute the correlation-length ratios for other types of AFM order instead of λ_8 , further verifying that only λ_8 -AFM long-range order is present in the ground state [55]. With varying magnetic flux ϕ , we implement a similar procedure and arrive at the ground-state phase diagram of the Eq. (4), as shown in Fig. 3a, in which U_c increases with ϕ .

After accessing the phase diagram, we investigate the critical properties. The data collapse analysis of $R_{\lambda_8\text{-AFM}}$ versus $(U - U_c)L^{1/\nu}$ in the regime close to QCP with fixed $\phi = 0.075$ gives $1/\nu = 0.68(5)$, as shown in Fig. 3c. Moreover, at U_c , the short-time dynamics of the structure factor $S_{\lambda_8\text{-AFM}}$ and the fermion correlation function G_f (defined in SM Sec. IV [55]) yield $\eta_\phi = 0.55(5)$ and $\eta_\psi = 0.15(3)$, as presented in Fig. 3d and 3e, respectively. To confirm the universality of this phase transition, we also evaluate the critical exponents for other values of ϕ , as presented in SM [55], which are consistent with each other within the error bar. Remarkably, the critical exponents found here are different from those of the Gross-Neveu universality classes [69, 70] (for comparison, see SM [55]), confirming that this phase transition belongs to a new universality class.

Concluding remarks — In summary, we establish an innovative theoretical framework to unravel critical properties in quantum many-body systems. The approach proposed in our work enables preempting the notorious sign problem in QMC by leveraging the short-stage imaginary-time relaxation dynamics. We demonstrate the accuracy and efficiency of the approach by systematically investigating several strongly interacting models by sign-problematic QMC. The comparison of our approach with conventional QMC shows that the sign problem is enormously reduced in our approach, thus largely reducing the computational time and enabling the accessing the numerically accurate critical exponents. For exam-

ple, for the SU(3) Hubbard model with $L = 10$, the estimated computational time in equilibrium QMC is millions of times that in our approach [55]. Consequently, our work paves a novel avenue to studying exotic QCP in quantum many-body systems, which are not amenable to the unbiased numerical approach previously.

More intriguingly, employing the newly developed approach, for the first time we reveal the ground-state properties of the staggered-flux SU(3) repulsive Hubbard model, and reveal a novel Dirac QCP different from previously known Gross-Neveu transitions. Our numerical studies motivate systematic theoretical analysis of the QCP in SU(3) Dirac fermions by field-theory approach. Moreover, the critical properties are potentially detectable in the synthetic quantum simulators such as optical lattice of cold atoms [61, 62]. Our results on the SU(3) Hubbard model provide theoretical guidance for the future experimental exploration of exotic physics in strongly correlated SU(N) Dirac fermions.

The basic procedure in our approach can be straightforwardly generalized to other fermionic QCP, including metallic QCP involving Fermi surface, for which the critical properties attract considerable attentions, but remain largely elusive. Additionally, we believe that short-time nonequilibrium QMC is also applicable in sign-problematic bosonic models. We should mention that in some specific cases, although sign problem is alleviated, it remains difficult to access the critical properties with large system size in our current simulation. For example, when staggered magnetic flux is large in SU(3) Hubbard model, even at short-time stage the sign problem is too severe to allow us reach the results with high accuracy close to the QCP. Nonetheless, bestowing the flexibility of the framework, it is feasible to further ameliorate the efficiency of our approach, for instance through improvement of initial state and optimization of H-S channel [31, 32], which is an interesting direction in future. We believe that our work promises a pathway towards a general strategy of studying the QCP in strongly correlated systems by unbiased numerical approach.

Acknowledgments — We acknowledge helpful discussions with Yiwen Pan. Yin-Kai Yu, Zhi-Xuan Li and Shuai Yin are supported by the National Natural Science Foundation of China (Grants No. 12222515 and No. 12075324). Zi-Xiang Li is supported by the NSFC under Grant No. 12347107. Shuai Yin is also supported by the Science and Technology Projects in Guangdong Province (Grants No. 2021QN02X561).

-
- [1] S. Sachdev, *Quantum Phase Transitions*, 2nd ed. (Cambridge Univ. Press, 2011).
 [2] J. Zaanen, *Science* **319**, 1205 (2008), <https://www.science.org/doi/pdf/10.1126/science.1152443>.
 [3] S. Weinberg, *The quantum theory of fields*, Vol. 1 (Cambridge university press, 1995).
 [4] R. Blankenbecler, D. J. Scalapino, and R. L. Sugar, *Phys.*

- Rev. D* **24**, 2278 (1981).
 [5] J. E. Hirsch, D. J. Scalapino, R. L. Sugar, and R. Blankenbecler, *Phys. Rev. Lett.* **47**, 1628 (1981).
 [6] J. E. Hirsch, *Phys. Rev. B* **31**, 4403 (1985).
 [7] E. Y. Loh, J. E. Gubernatis, R. T. Scalettar, S. R. White, D. J. Scalapino, and R. L. Sugar, *Phys. Rev. B* **41**, 9301 (1990).

- [8] P. Henelius and A. W. Sandvik, *Phys. Rev. B* **62**, 1102 (2000).
- [9] M. Troyer and U.-J. Wiese, *Phys. Rev. Lett.* **94**, 170201 (2005).
- [10] M. B. Hastings, *Journal of Mathematical Physics* **57**, 015210 (2015), https://pubs.aip.org/aip/jmp/article-pdf/doi/10.1063/1.4936216/11140394/015210_1.online.pdf.
- [11] Z. Ringel and D. L. Kovrizhin, *Science Advances* **3**, e1701758 (2017), <https://www.science.org/doi/pdf/10.1126/sciadv.1701758>.
- [12] D. P. Arovas, E. Berg, S. A. Kivelson, and S. Raghu, *Annual Review of Condensed Matter Physics* **13**, 239 (2022).
- [13] M. Qin, T. Schäfer, S. Andergassen, P. Corboz, and E. Gull, *Annual Review of Condensed Matter Physics* **13**, 275 (2022).
- [14] T. DeGrand and C. DeTar, *Lattice Methods for Quantum Chromodynamics* (WORLD SCIENTIFIC, 2006) <https://www.worldscientific.com/doi/pdf/10.1142/6065>.
- [15] Z.-X. Li and H. Yao, *Annual Review of Condensed Matter Physics* **10**, 337 (2019), <https://doi.org/10.1146/annurev-conmatphys-033117-054307>.
- [16] S. Chandrasekharan and U.-J. Wiese, *Phys. Rev. Lett.* **83**, 3116 (1999).
- [17] E. F. Huffman and S. Chandrasekharan, *Phys. Rev. B* **89**, 111101 (2014).
- [18] C. Wu and S.-C. Zhang, *Phys. Rev. B* **71**, 155115 (2005).
- [19] E. Berg, M. A. Metlitski, and S. Sachdev, *Science* **338**, 1606 (2012), <https://www.science.org/doi/pdf/10.1126/science.1227769>.
- [20] Z.-X. Li, Y.-F. Jiang, and H. Yao, *Physical Review B* **91**, 241117 (2015).
- [21] Z.-X. Li, Y.-F. Jiang, and H. Yao, *Physical Review Letters* **117**, 267002 (2016).
- [22] S. Zhang and H. Krakauer, *Phys. Rev. Lett.* **90**, 136401 (2003).
- [23] L. Wang, Y.-H. Liu, M. Iazzi, M. Troyer, and G. Harcos, *Phys. Rev. Lett.* **115**, 250601 (2015).
- [24] Z. C. Wei, C. Wu, Y. Li, S. Zhang, and T. Xiang, *Phys. Rev. Lett.* **116**, 250601 (2016).
- [25] R. Mondaini, S. Tarat, and R. T. Scalettar, *Science* **375**, 418 (2022).
- [26] D. Hangleiter, I. Roth, D. Nagaj, and J. Eisert, *Science Advances* **6**, eabb8341 (2020), <https://www.science.org/doi/pdf/10.1126/sciadv.abb8341>.
- [27] R. Levy and B. K. Clark, *Phys. Rev. Lett.* **126**, 216401 (2021).
- [28] Z.-Y. Han, Z.-Q. Wan, and H. Yao, Pfaffian quantum monte carlo: solution to majorana sign ambiguity and applications (2024), [arXiv:2408.10311 \[cond-mat.str-el\]](https://arxiv.org/abs/2408.10311).
- [29] A. Alexandru, G. m. c. Bařar, P. F. Bedaque, and N. C. Warrington, *Rev. Mod. Phys.* **94**, 015006 (2022).
- [30] O. Golan, A. Smith, and Z. Ringel, *Phys. Rev. Res.* **2**, 043032 (2020).
- [31] W.-X. Chang and Z.-X. Li, *Phys. Rev. B* **110**, 085152 (2024).
- [32] Z.-Q. Wan, S.-X. Zhang, and H. Yao, *Phys. Rev. B* **106**, L241109 (2022).
- [33] X. Zhang, G. Pan, X. Y. Xu, and Z. Y. Meng, *Phys. Rev. B* **106**, 035121 (2022).
- [34] T. Sato and F. F. Assaad, *Phys. Rev. B* **104**, L081106 (2021).
- [35] M.-S. Vaezi, A.-R. Negari, A. Moharramipour, and A. Vaezi, *Phys. Rev. Lett.* **127**, 217003 (2021).
- [36] O. Grossman and E. Berg, *Phys. Rev. Lett.* **131**, 056501 (2023).
- [37] S. L. Sondhi, S. M. Girvin, J. P. Carini, and D. Shahar, *Rev. Mod. Phys.* **69**, 315 (1997).
- [38] M. Vojta, *Reports on Progress in Physics* **66**, 2069 (2003).
- [39] J. A. Hertz, *Phys. Rev. B* **14**, 1165 (1976).
- [40] A. J. Millis, *Phys. Rev. B* **48**, 7183 (1993).
- [41] E. Berg, S. Lederer, Y. Schattner, and S. Trebst, *Annual Review of Condensed Matter Physics* **10**, 63 (2019), <https://doi.org/10.1146/annurev-conmatphys-031218-013339>.
- [42] D. J. Scalapino, *Rev. Mod. Phys.* **84**, 1383 (2012).
- [43] P. A. Lee, N. Nagaosa, and X.-G. Wen, *Rev. Mod. Phys.* **78**, 17 (2006).
- [44] S. Lederer, Y. Schattner, E. Berg, and S. A. Kivelson, *Phys. Rev. Lett.* **114**, 097001 (2015).
- [45] C. M. Varma, *Rev. Mod. Phys.* **92**, 031001 (2020).
- [46] P. W. Phillips, N. E. Hussey, and P. Abbamonte, *Science* **377**, eabh4273 (2022), <https://www.science.org/doi/pdf/10.1126/science.abh4273>.
- [47] H. K. Janssen, B. Schaub, and B. Schmittmann, *Zeitschrift für Physik B Condensed Matter* **73**, 539 (1989).
- [48] Z. B. Li, L. Schülke, and B. Zheng, *Phys. Rev. Lett.* **74**, 3396 (1995).
- [49] S. Yin, P. Mai, and F. Zhong, *Phys. Rev. B* **89**, 144115 (2014).
- [50] Y.-K. Yu, Z. Zeng, Y.-R. Shu, Z.-X. Li, and S. Yin, Nonequilibrium dynamics in dirac quantum criticality (2023), [arXiv:2310.10601 \[cond-mat.str-el\]](https://arxiv.org/abs/2310.10601).
- [51] F. Assaad and H. Evertz, World-line and determinantal quantum monte carlo methods for spins, phonons and electrons, in *Computational Many-Particle Physics* (Springer Berlin Heidelberg, Berlin, Heidelberg, 2008) pp. 277–356.
- [52] S. M. Tabatabaei, A.-R. Negari, J. Maciejko, and A. Vaezi, *Phys. Rev. Lett.* **128**, 225701 (2022).
- [53] Z.-X. Li, A. Vaezi, C. B. Mendl, and H. Yao, *Science Advances* **4**, eaau1463 (2018), <https://www.science.org/doi/pdf/10.1126/sciadv.aau1463>.
- [54] T. C. Lang and A. M. Läuchli, *Physical Review Letters* **123**, 137602 (2019).
- [55] See Supplementary Materials at [URL will be inserted by publisher] for more details of nonequilibrium PQMC simulation and more details of the three fermion models in this study.
- [56] G. P. Vacca and L. Zambelli, *Phys. Rev. D* **91**, 125003 (2015).
- [57] L. Wang, P. Corboz, and M. Troyer, *New Journal of Physics* **16**, 103008 (2014).
- [58] Z.-X. Li, Y.-F. Jiang, and H. Yao, *New Journal of Physics* **17**, 085003 (2015).
- [59] S. Hesselmann and S. Wessel, *Phys. Rev. B* **93**, 155157 (2016).
- [60] Z.-X. Li, Z.-Q. Wan, and H. Yao, Asymptotic sign free in interacting fermion models (2022), [arXiv:2211.00663 \[cond-mat.str-el\]](https://arxiv.org/abs/2211.00663).
- [61] H. Ozawa, S. Taie, Y. Takasu, and Y. Takahashi, *Phys. Rev. Lett.* **121**, 225303 (2018).
- [62] S. Taie, E. Ibarra-Garcia-Padilla, N. Nishizawa, Y. Takasu, Y. Kuno, H.-T. Wei, R. T. Scalettar, K. R. A. Hazzard, and Y. Takahashi, *Nature Physics* **18**, 1356 (2022).

- [63] T. C. Lang, Z. Y. Meng, A. Muramatsu, S. Wessel, and F. F. Assaad, *Physical Review Letters* **111**, 066401 (2013), arXiv:1306.3258 [cond-mat].
- [64] Z. Zhou, D. Wang, Z. Y. Meng, Y. Wang, and C. Wu, *Physical Review B* **93**, 245157 (2016), arXiv:1512.03994 [cond-mat].
- [65] Y.-Y. He, H.-Q. Wu, Y.-Z. You, C. Xu, Z. Y. Meng, and Z.-Y. Lu, *Phys. Rev. B* **94**, 241111 (2016).
- [66] Z.-X. Li, Y.-F. Jiang, S.-K. Jian, and H. Yao, *Nature Communications* **8**, 314 (2017).
- [67] H. Xu, X. Li, Z. Zhou, X. Wang, L. Wang, C. Wu, and Y. Wang, *Phys. Rev. Res.* **5**, 023180 (2023).
- [68] M. Gell-Mann, *Phys. Rev.* **125**, 1067 (1962).
- [69] B. Rosenstein, Hoi-Lai Yu, and A. Kovner, *Phys. Lett. B* **314**, 381 (1993).
- [70] L. Janssen and I. F. Herbut, *Phys. Rev. B* **89**, 205403 (2014).
- [71] Y. Otsuka, K. Seki, S. Sorella, and S. Yunoki, *Physical Review B* **102**, 235105 (2020).
- [72] G. Cassella, P. d'Ornellas, T. Hodson, W. M. H. Natori, and J. Knolle, *Nature Communications* **14**, 6663 (2023).
- [73] D. E. Burlankov, *Theoretical and Mathematical Physics* **138**, 78 (2004).
- [74] R. Gilmore, *Journal of Geometry and Symmetry in Physics* **28**, 1 (2012).

Supplementary Materials for

Preempting Fermion Sign Problem: Unveiling Quantum Criticality through Nonequilibrium Dynamics

CONTENTS

I. Details of nonequilibrium imaginary-time dynamics in PQMC simulation	9
A. Imaginary-time relaxation dynamics simulated by PQMC	9
B. Hubbard-Stratonovich transformation	9
C. Sign problem in PQMC	10
II. More details for the single-Dirac-fermion Hubbard model	10
A. Sign problem behaviors	10
B. Verification of the QCP and critical exponents	11
III. More details for the spinless t - V model	12
A. Sign problem behaviors	12
B. Verification of the QCP and critical exponents	13
IV. More details for the SU(3) Hubbard model	14
A. SU(3) algebra	14
B. Mean-field analyses	15
C. Phase boundary and critical exponents	17
D. The new universality class	19
E. Sign problem behaviors and computational efficiency	20

I. DETAILS OF NONEQUILIBRIUM IMAGINARY-TIME DYNAMICS IN PQMC SIMULATION

A. Imaginary-time relaxation dynamics simulated by PQMC

We focus on the imaginary-time relaxation dynamics from a fully ordered or Dirac semimetal initial state $|\psi_0\rangle$. The initial state is prepared by solving $H_0|\psi_0\rangle = E_0|\psi_0\rangle$, where H_0 is the initial Hamiltonian and E_0 is the ground state energy. With these initial states, the evolution of the observable $O(\tau)$ is given by

$$\langle O(\tau) \rangle = \frac{\langle \psi_0 | e^{-\frac{\tau}{2}H} O e^{-\frac{\tau}{2}H} | \psi_0 \rangle}{\langle \psi_0 | e^{-\tau H} | \psi_0 \rangle}. \quad (\text{S1})$$

As $\tau \rightarrow \infty$, $e^{-\frac{\tau}{2}H}$ projects the system onto the ground state of H .

The imaginary-time relaxation dynamics can be simulated via the projector quantum Monte Carlo (PQMC) [51]. In conventional PQMC studies, a sufficiently large τ (usually τ should be several times as large as L) is needed to ensure that the ground state is obtained. Then the physical quantities are calculated in the ground state. In contrast, in our work, we focus on the short-time stage of the imaginary-time relaxation process, and τ does not need to be very large compared with L .

B. Hubbard-Stratonovich transformation

In the PQMC simulations, the interaction terms in the form of four-fermion operators should be decoupled via Hubbard-Stratonovich (HS) transformation. We at first use the Trotter decomposition to discretize the imaginary-time evolution operator into $M = \tau/\Delta\tau$ (where M is an integer) time slices, i.e.,

$$e^{-\tau H} = \prod_{m=1}^M [e^{-\Delta\tau H_t} e^{-\Delta\tau H_U} + \mathcal{O}(\Delta\tau^2)], \quad (\text{S2})$$

where H_t and H_U represent the free fermion hopping term and the interaction term in the Hamiltonian, respectively. Then, we use the HS transformation on H_U to decouple the fermion-fermion interaction into interactions between non-interacting fermions and auxiliary fields.

For the single-Dirac-fermion Hubbard model, we use the following HS transformation:

$$e^{-\Delta\tau U(n_{i\uparrow} - \frac{1}{2})(n_{i\downarrow} - \frac{1}{2})} = \frac{1}{2} e^{-\frac{\Delta\tau U}{4}} \sum_{s_i = \pm 1} e^{\lambda s_i (c_{i\uparrow}^\dagger c_{i\downarrow} + c_{i\downarrow}^\dagger c_{i\uparrow})}. \quad (\text{S3})$$

where $\cosh \lambda = e^{\frac{\Delta\tau U}{2}}$. For $U > 0$ (Hubbard repulsive interaction), the sign problem arises for all channels. We here choose the σ_x channel to mitigate the sign problem [52].

For the spinless t - V model, previous studies have shown that at half-filling, the model can be decoupled into the hopping channel without the sign problem, which has been demonstrated from various perspectives [20, 21, 23, 24]. In our study, however, we use the HS transformation in a sign-problematic channel, namely the density channel:

$$e^{-\Delta\tau V(n_i - \frac{1}{2})(n_j - \frac{1}{2})} = \frac{1}{2} e^{-\frac{\Delta\tau V}{4}} \sum_{s_{ij} = \pm 1} e^{\lambda s_{ij} (n_i - n_j)}. \quad (\text{S4})$$

where $\cosh \lambda = e^{\frac{\Delta\tau V}{2}}$. Despite the presence of sign problem, the numerical results we obtained are consistent with the previously established results, demonstrating the reliability of our new method.

For the SU(3) repulsive Hubbard model, we use the following HS transformation:

$$e^{\Delta\tau \frac{U}{2} (n_{i\alpha} - n_{i\beta})^2} = \frac{1}{2} \sum_{s_i = \pm 1} e^{\lambda s_i (n_{i\alpha} - n_{i\beta})}. \quad (\text{S5})$$

where $\cosh \lambda = e^{\frac{\Delta\tau U}{2}}$. For all the known algorithms, the SU(3) repulsive Hubbard model is sign-problematic for any decoupling channel in HS transformation.

C. Sign problem in PQMC

Through the HS transformation, the Hamiltonian can be converted into a quadratic effective form of fermionic operators that depends on the spacetime configuration of the auxiliary fields. The partition function can then be expressed as a sum of configuration weight $w(c)$, i.e., $Z = \sum_c w(c)$. These weights are given by the determinant of the effective Hamiltonian of fermions [51].

In PQMC simulations, we sample the space-time dependent configuration of the auxiliary field. For sign-free models, the sampling probability is proportional to the configuration weight $w(c)$. However, for the sign-problematic models, the configuration weight $w(c)$ is not positive definite, so it cannot be used directly as the sampling probability. Instead, the absolute value $|w(c)|$ is used as the sampling probability, and the observables are computed as follows [9, 15]:

$$\langle O \rangle = \frac{\sum_c w(c) O(c)}{\sum_c w(c)} = \frac{\sum_c |w(c)| \text{sign}(c) O(c) / \sum_c |w(c)|}{\sum_c |w(c)| \text{sign}(c) / \sum_c |w(c)|} = \frac{\langle O \rangle_{|w|}}{\langle \text{sign} \rangle_{|w|}}. \quad (\text{S6})$$

Here, we have used

$$\langle \square \rangle_{|w|} = \frac{\sum_c \square |w(c)|}{\sum_c |w(c)|}, \quad (\text{S7})$$

to denote the expectation value obtained using $|w(c)|$ as the sampling probability. The sign problem introduces a cost that the average sign $\langle \text{sign} \rangle_{|w|}$ tends to zero due to the frequent cancellation of positive and negative weights across different configurations, leading to the consequence that (S6) becomes a ratio between two tiny numbers. This is numerically unstable and introduces significant statistical errors. Specifically, it is proven that the error generally follows [9]:

$$\Delta \langle O \rangle \propto \frac{1}{\langle \text{sign} \rangle_{|w|}} \propto e^{\tau N \Delta f}, \quad (\text{S8})$$

where Δf denotes the difference in the free energy density between the actual fermionic system and its corresponding bosonic system. The exponential dependence of the error amplification factor on the imaginary time τ and the number of particles N means that QMC requires exponentially long computational times to achieve controllable statistical errors when solving ground-state problems of quantum systems in the thermodynamic limit.

In subsequent analyses, we use the average sign $\langle \text{sign} \rangle_{|w|}$ to measure the severity of the sign problem. The lower value of the average sign $\langle \text{sign} \rangle_{|w|}$ indicates a more severe sign problem.

II. MORE DETAILS FOR THE SINGLE-DIRAC-FERMION HUBBARD MODEL

A. Sign problem behaviors

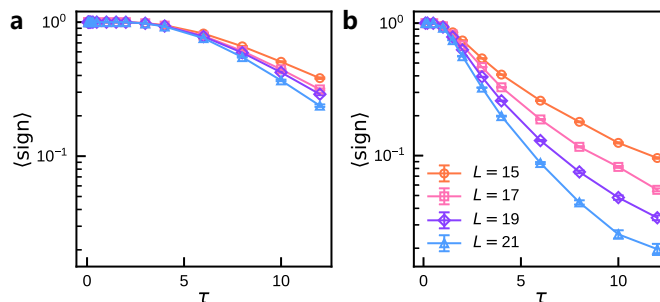


FIG. S1. **Evolution of the average sign at the critical point.** **a**, Evolution from the DSM initial state. **b**, Evolution from the FM initial state.

Fig. S1 shows that near the critical point of the single-Dirac-fermion Hubbard model, the average sign $\langle \text{sign} \rangle$ decays in the imaginary-time relaxation with the Dirac semimetal (DSM) and the ferromagnetic (FM) initial states. We find that different initial states can have different decay rates. In the relaxation with the DSM initial state, the average sign decays more slowly. The data presented in Fig. 1 of the main text show the relaxation results starting from the DSM initial state.

B. Verification of the QCP and critical exponents

Several physical quantities are needed to describe the universal scaling behaviors near the QCP. The ferromagnetic structure factor S_{FM} is defined as

$$S_{\text{FM}}(\mathbf{k}) \equiv \frac{1}{L^{2d}} \sum_{i,j} e^{i\mathbf{k}\cdot(\mathbf{r}_i - \mathbf{r}_j)} \langle S_i^z S_j^z \rangle, \quad (\text{S9})$$

where the local spin operator is $S_i^z \equiv \mathbf{c}_i^\dagger \sigma^z \mathbf{c}_i$ with $\mathbf{c}^\dagger \equiv (c_\uparrow^\dagger, c_\downarrow^\dagger)$. In addition, the correlation length ratio R_{FM} is defined as

$$R_{\text{FM}} \equiv 1 - \frac{S_{\text{FM}}(\mathbf{k} = \Delta\mathbf{k})}{S_{\text{FM}}(\mathbf{k} = 0)}, \quad (\text{S10})$$

where $\Delta\mathbf{k} = \frac{1}{L}\mathbf{b}_1 + \frac{1}{L}\mathbf{b}_2$ is the minimum momentum of electrons in a lattice with periodic boundary conditions, and $\mathbf{b}_1, \mathbf{b}_2$ are the reciprocal lattice vectors. The fermion correlation function $G_f(\mathbf{k})$ is defined as

$$G_f(\mathbf{k}) \equiv \frac{1}{L^2} \sum_{ij} e^{i\mathbf{k}\cdot(\mathbf{r}_i - \mathbf{r}_j)} \langle c_{i\uparrow}^\dagger c_{j\downarrow} \rangle. \quad (\text{S11})$$

In the main text and figures of data, we abbreviate $S_{\text{FM}} \equiv S_{\text{FM}}(\mathbf{k} = \mathbf{0})$ and $G_f \equiv G_f(\mathbf{k} = \Delta\mathbf{k})$, unless otherwise specified.

The correlation length ratio R_{FM} is a dimensionless quantity. In the nonequilibrium critical region, the correlation length ratio R_{FM} satisfies the following scaling form:

$$R_{\text{FM}}(g, \tau, L) = f_R(gL^{1/\nu}, \tau L^{-z}), \quad (\text{S12})$$

where $g = U - U_c$. To determine the quantum critical point U_c , we fix τL^{-z} to be constant (e.g., we take $\tau L^{-z} = 0.3$ in the main text), so the scaling form of R_{FM} reduces to $R(g, \tau, L) = f_{R1}(gL^{1/\nu})$, which is similar to the traditional finite-size scaling. Accordingly, the critical point can be determined by the intersection of curves of R_{FM} versus U for different L . We fit U_c and ν based on the expansion of the scaling form:

$$R_{\text{FM}}(g, L) = f_{R1}(gL^{1/\nu}) = \sum_{n=0}^{n_{\text{max}}} a_n g^n L^{n/\nu}. \quad (\text{S13})$$

where we appropriately truncate the scaling functions with polynomials [54].

In the main text, based on the results from the DSM initial state, we fit according to Eq. (S13) and obtain $U_c = 7.220(37)$ and $1/\nu = 1.18(3)$. Here we supplement with results from the FM initial state, as shown in Fig. S2. Using the same procedure (here we take $\tau L^{-z} = 0.5$), we fit according to Eq. (S13) and obtain $U_c = 7.214(44)$ and $1/\nu = 1.05(10)$, which are close to the results from the DSM initial state. These results not only confirm the values of the critical point U_c and the critical exponent $1/\nu$, but also show that the initial states can be chosen flexibly in our method, which provides a route to achieve reliable values of critical exponents by benchmarking the results with different initial states.

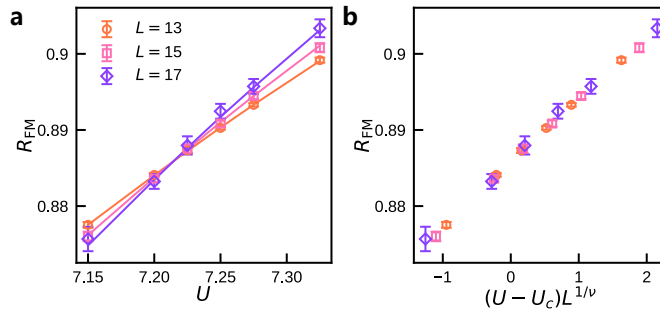


FIG. S2. **Verification of the quantum criticality with FM initial state at $\tau = 0.5L^z$.** **a**, Curves of R_{FM} versus U intersect for different L . **b**, Data collapse after rescaling with $1/\nu = 1.18(3)$.

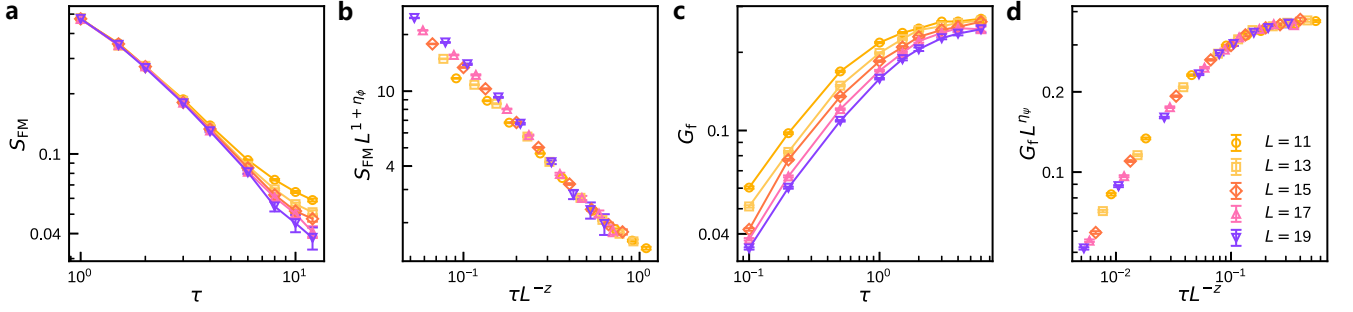


FIG. S3. **Relaxation dynamics at QCP with FM initial state in single-Dirac-fermion Hubbard model.** **a-b**, Curves of $S_{\text{FM}} \equiv S_{\text{FM}}(\mathbf{k} = \mathbf{0})$ versus τ for different sizes before and after rescaling. **c-d**, Curves of $G_{\text{f}} \equiv G_{\text{f}}(\mathbf{k} = \Delta\mathbf{k})$ versus τ before and after rescaling. Data collapse in the relaxation dynamics shows $\eta_{\phi} = 0.34(5)$ and $\eta_{\psi} = 0.131(20)$.

The anomalous dimensions of the bosonic field η_{ϕ} and the fermionic field η_{ψ} can be determined by the following scaling relations:

$$S_{\text{FM}}(\mathbf{k} = \mathbf{0}) = L^{-(1+\eta_{\phi})} f_S(gL^{1/\nu}, \tau L^{-z}), \quad (\text{S14})$$

$$G_{\text{f}}(\mathbf{k} = \Delta\mathbf{k}) = L^{-\eta_{\psi}} f_G(gL^{1/\nu}, \tau L^{-z}). \quad (\text{S15})$$

We obtain $\eta_{\phi} = 0.34(5)$ and $\eta_{\psi} = 0.131(20)$ from the data collapse in the relaxation dynamics at $g = 0$, as shown in Fig. S3.

Table S1 compares the results in the present work with those of other methods. The consistent results shown in this table demonstrate that the method based on the short-time dynamics can accurately determine the critical properties of the ground-state QCP with much fewer computational costs.

TABLE S1. **Comparison of critical properties for the single-Dirac-fermion Hubbard model calculated by different methods.** The method used in this work is the nonequilibrium short-time PQMC.

Methods	U_c	ν^{-1}	η_{ϕ}	η_{ψ}
This work (from DSM, $\tau = 0.3L^z$)	7.220(37)	1.18(3)	0.33(2)	0.135(2)
This work (from FM, $\tau = 0.5L^z$)	7.214(44)	1.05(10)	0.34(5)	0.131(20)
Gutzwiller-PQMC (equilibrium) [52]	7.275(25)	1.19(3)	0.31(1)	0.136(5)
FRG [56]	-	1.229	0.372	0.131

III. MORE DETAILS FOR THE SPINLESS t - V MODEL

A. Sign problem behaviors

As shown in Fig. S4, for both DSM initial state and CDW initial state, the average sign in the short-time stage is close to one, indicating the sign problem is very weak. In particular, for $\tau = 0.3L^z$, as shown in the insets of Fig. S4, the system almost remains sign-free near the critical point $V_c = 1.35(1)$ determined in the main text.

Incidentally, Fig. S4 shows that the decay rate of $\langle \text{sign} \rangle$ does not monotonically change with the system size L . In some cases, a larger system size L results in a weaker sign problem. Such phenomena have also been reported in the equilibrium QMC study [60].

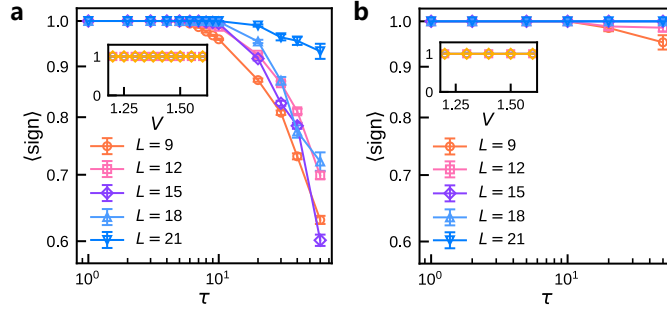


FIG. S4. **Evolution of average sign at the QCP (inset shows $\langle \text{sign} \rangle$ versus V near the QCP for $\tau = 0.3L^z$).** **a**, Evolution from the DSM initial state. **b**, Evolution from the CDW initial state.

B. Verification of the QCP and critical exponents

For this model, the ordered phase is the charge density wave (CDW) state, for which the structure factor S_{CDW} can be defined as:

$$S_{\text{CDW}}(\mathbf{k}) \equiv \frac{1}{L^{2d}} \sum_{i,j} e^{i\mathbf{k} \cdot (\mathbf{r}_i - \mathbf{r}_j)} \langle m_i m_j \rangle, \quad (\text{S16})$$

where the local order operator is $m_i \equiv \frac{1}{2}(n_{i,A} - n_{i,B})$, which represents the difference in particle number density between the two sublattices in a unit cell. The associated correlation length ratio R_{CDW} is defined as:

$$R_{\text{CDW}} \equiv 1 - \frac{S_{\text{CDW}}(\mathbf{k} = \Delta\mathbf{k})}{S_{\text{CDW}}(\mathbf{k} = 0)}. \quad (\text{S17})$$

The fermion correlation $G_f(\mathbf{k})$ is defined similarly to Eq. (S11):

$$G_f(\mathbf{k}) \equiv \frac{1}{L^2} \sum_{ij} e^{i\mathbf{k} \cdot (\mathbf{r}_i - \mathbf{r}_j)} \langle c_{i,A}^\dagger c_{j,B} \rangle. \quad (\text{S18})$$

Here, the sublattice indices A and B function as Dirac spinor indices. In the main text and figures of data, we abbreviate $S_{\text{FM}} \equiv S_{\text{FM}}(\mathbf{k} = \mathbf{0})$ and $G_f \equiv G_f(\mathbf{k} = \mathbf{K} + \Delta\mathbf{k})$, where $\mathbf{K} = (\pm\frac{4\pi}{3}, 0)$ represents the momentum at the Dirac points.

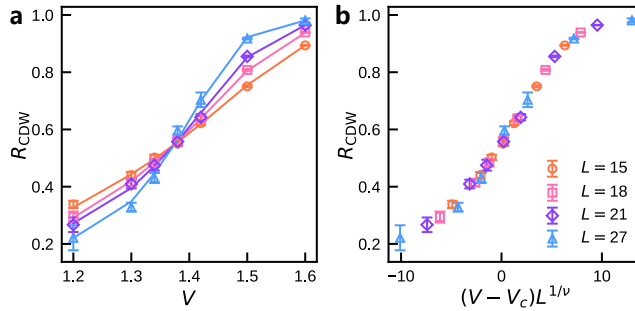


FIG. S5. **Determination of the critical point and $1/\nu$ with DSM initial state.** **a**, At $\tau = 0.3L^z$, curves of R_{CDW} versus V for different sizes intersect at $V_c = 1.37(2)$. **b**, Data collapse of curves of R_{CDW} versus rescaled $(V - V_c)L^{1/\nu}$ with $\nu = 0.79(5)$.

In Fig. 2 of the main text, we showed the results of determination of critical properties via the short-time dynamics from the ordered CDW initial state. In contrast, here we show consistent results can also be obtained from the DSM initial state.

Fig. S5 illustrates the correlation length ratio R_{CDW} as a function of interaction strength V at $\tau = 0.3L^z$. We fit the data in Fig. S5a using the scaling form in Eq. S13, determining the intersection point of the curves for different sizes as $V_c = 1.37(2)$ and the scaling collapse exponent as $\nu = 0.79(5)$. These results are close to those obtained

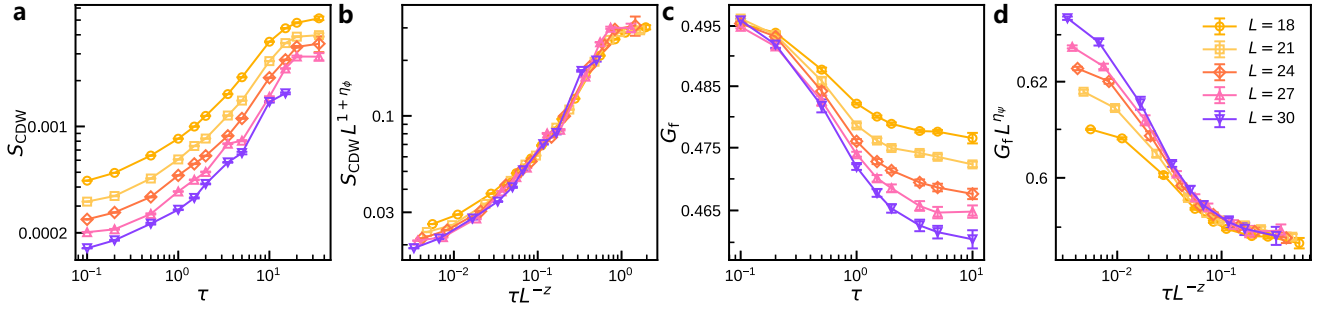


FIG. S6. **Relaxation dynamics at QCP with DSM initial state in spinless t - V model.** **a-b**, Curves of $S_{\text{CDW}} \equiv S_{\text{CDW}}(\mathbf{k} = \mathbf{0})$ versus τ for different sizes before and after rescaling. **c-d**, Curves of $G_f \equiv G_f(\mathbf{k} = \mathbf{K} + \Delta\mathbf{k})$ versus τ before and after rescaling. Data collapse in the relaxation dynamics shows $\eta_\phi = 0.44(2)$ and $\eta_\psi = 0.072(4)$.

by equilibrium methods [57, 58] and the short-time dynamics with ordered CDW initial state discussed in the main text. Fig. S6 shows the relaxation dynamics of $S_{\text{CDW}} = S_{\text{CDW}}(\mathbf{k} = \mathbf{0})$ and $G_f = G_f(\mathbf{k} = \mathbf{K} + \Delta\mathbf{k})$ starting from the DSM initial state. Their scaling behavior is described by Eq. (S14) and Eq. (S15). According to the scaling collapse of the evolution of S_{CDW} in Fig. S6a-S6b, one finds $\eta_\phi = 0.44(2)$. In addition, from the scaling collapse of the evolution of G_f in Fig. S6c-S6d, we obtain $\eta_\psi = 0.072(4)$. The value of η_ϕ is close to that obtained by the equilibrium methods [57, 58] and the short-time dynamics with ordered CDW initial state discussed in the main text; while the value of η_ψ is close to the FRG result [56], and also consistent with that obtained from the CDW initial state shown in the main text. Consequently, the results of critical properties in the t - V model further demonstrate the efficiency and accuracy of our method. More crucially, for the first time, through our method we achieve the reliable result of fermionic anomalous dimension η_ψ for the QCP in the spinless t - V model by unbiased QMC simulation, as shown in Table S2.

TABLE S2. **Comparison of critical properties for the spinless t - V model calculated by different methods.** The method used in this work is the nonequilibrium short-time PQMC.

Methods	U_c	ν	η_ϕ	η_ψ
This work (from CDW, $\tau = 0.3L^z$)	1.35(1)	0.77(12)	0.49(5)	0.073(4)
This work (from DSM, $\tau = 0.3L^z$)	1.37(2)	0.79(5)	0.44(2)	0.072(4)
Majorana QMC (equilibrium) [58]	1.355(1)	0.77(2)	0.45(2)	-
Continuous-time QMC (equilibrium) [57]	1.356(1)	0.80(3)	0.302(7)	-
FRG [56]	-	0.929	0.602	0.069

IV. MORE DETAILS FOR THE SU(3) HUBBARD MODEL

A. SU(3) algebra

The SU(3) Hubbard model with staggered flux is invariant under SU(3) transformations in the flavor space of fermions. Here we give a brief review on the SU(3) algebra.

The generators of the SU(3) group are represented by the well-known Gell-Mann matrices. Below are the eight

Gell-Mann matrices, corresponding to the generators of SU(3) group:

$$\begin{aligned}
\lambda_1 &= \begin{pmatrix} 0 & 1 & 0 \\ 1 & 0 & 0 \\ 0 & 0 & 0 \end{pmatrix}, & \lambda_2 &= \begin{pmatrix} 0 & -i & 0 \\ i & 0 & 0 \\ 0 & 0 & 0 \end{pmatrix}, & \lambda_3 &= \begin{pmatrix} 1 & 0 & 0 \\ 0 & -1 & 0 \\ 0 & 0 & 0 \end{pmatrix}, \\
\lambda_4 &= \begin{pmatrix} 0 & 0 & 1 \\ 0 & 0 & 0 \\ 1 & 0 & 0 \end{pmatrix}, & \lambda_5 &= \begin{pmatrix} 0 & 0 & -i \\ 0 & 0 & 0 \\ i & 0 & 0 \end{pmatrix}, & \lambda_6 &= \begin{pmatrix} 0 & 0 & 0 \\ 0 & 0 & 1 \\ 0 & 1 & 0 \end{pmatrix}, \\
\lambda_7 &= \begin{pmatrix} 0 & 0 & 0 \\ 0 & 0 & -i \\ 0 & i & 0 \end{pmatrix}, & \lambda_8 &= \begin{pmatrix} 1/\sqrt{3} & 0 & 0 \\ 0 & 1/\sqrt{3} & 0 \\ 0 & 0 & -2/\sqrt{3} \end{pmatrix}.
\end{aligned} \tag{S19}$$

The Lie algebra structure of the SU(3) group is determined by the commutation relations of its generators. The commutation relations between the generators of the SU(3) group are listed as follows:

$$[\lambda_a, \lambda_b] = 2i \sum_c f_{abc} \lambda_c, \tag{S20}$$

where f_{abc} are the structure constants, specifically:

$$f_{123} = 1, \tag{S21}$$

$$f_{147} = f_{246} = f_{257} = f_{345} = \frac{1}{2}, \tag{S22}$$

$$f_{156} = f_{367} = -\frac{1}{2}, \tag{S23}$$

$$f_{458} = f_{678} = \frac{\sqrt{3}}{2}. \tag{S24}$$

These commutation relations will determine the manifold shape of the ground-state degeneracy space of the ordered phase, which we will further analyze with numerical evidence in the subsequent sections.

B. Mean-field analyses

To qualitatively understand the salient features of ground-state phase diagram and the dominant symmetry spontaneous breaking ordering in the SU(3) Hubbard model, we first perform a mean-field analysis. We rewrite the interaction term in the following form and apply the mean-field approximation:

$$\begin{aligned}
\frac{U}{2} \sum_i \left(\sum_\alpha n_{i\alpha} - \frac{3}{2} \right)^2 &= \frac{U}{2} \sum_i \sum_{\alpha, \alpha'} n_{i\alpha} n_{i\alpha'} + \text{const.} \\
&= -\frac{U}{4} \sum_i \sum_{\alpha, \alpha'} (n_{i\alpha} - n_{i\alpha'})^2 + \text{const.} \\
&= -\frac{3U}{16} \sum_i \sum_n \left(\mathbf{c}_i^\dagger \lambda_n \mathbf{c}_i \right)^2 + \text{const.} \\
&\approx -\frac{3U}{16} \sum_n \langle m_{\lambda_n\text{-AFM}} \rangle \sum_i (-1)^i \mathbf{c}_i^\dagger \lambda_n \mathbf{c}_i + \text{const.},
\end{aligned} \tag{S25}$$

where $\mathbf{c}_i^\dagger \equiv (\mathbf{c}_{i1}^\dagger \ \mathbf{c}_{i2}^\dagger \ \mathbf{c}_{i3}^\dagger)$, and $\lambda_n = (\lambda_1, \lambda_2, \dots, \lambda_8)$ are the eight Gell-Mann matrices. The mean-field order parameter is defined as

$$\langle m_{\lambda_n\text{-AFM}} \rangle \equiv \frac{1}{L^2} \sum_i (-1)^i \langle \mathbf{c}_i^\dagger \lambda_n \mathbf{c}_i \rangle \tag{S26}$$

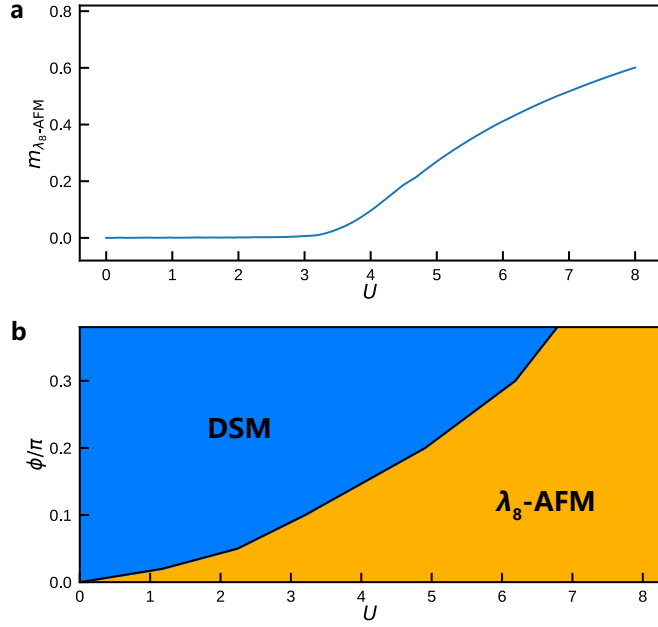


FIG. S7. **Mean-field results for the λ_8 -AFM order.** **a**, For $\phi = 0.1\pi, L = 30$, a DSM-AFM transition in the mean-field approximation is seen at $U = 3.20(1)$. **b**, Mean-field phase diagram with $L = 30$.

After applying the mean-field approximation, the Hamiltonian is entirely expressed as a quadratic form of fermionic operators and can be solved for the ground state using exact diagonalization. The problem is then simply reduced to a self-consistent calculation of the order parameter $\{m_n\}$. Fig. S7a shows the variation of the order parameter m_8 with interaction strength U calculated using the mean-field method. When the interaction is strong, m_8 starts to increase with U , showing clear characteristics of a continuous phase transition. We control different magnetic flux ϕ to find the corresponding phase boundary U , as shown in the mean-field phase diagram in Fig. S7b.

We can understand why the λ_8 -AFM order is preferred by examining the ground state energy of the system. Consider placing the eight different order parameter operators in the same external field h :

$$H_n^{\text{sat}} = -h \sum_i (-1)^i c_i^\dagger \lambda_n c_i, \quad (\text{S27})$$

whose ground state corresponds to the saturated λ_n -AFM ordered state. At half-filling, the ground state energy of $H_8^{\text{sat}}(h)$ is $-\frac{2}{\sqrt{3}}hL^2$. The energy gap at half-filling, between the ground state of $H_8^{\text{sat}}(h)$ and the first excited state of $H_8^{\text{sat}}(h)$, is a finite value $\frac{2}{\sqrt{3}}h$. For $H_{n \neq 8}^{\text{sat}}(h)$, the ground state energy is $-hL^2$ and the energy gap is 0. In other words, even considering the saturated ordered state, only the λ_8 -AFM order can open a gap in Dirac fermions, while other types of λ_n -AFM cannot.

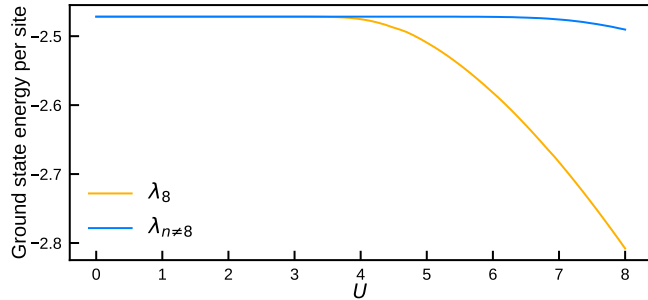


FIG. S8. **Mean-field ground state energy per site at half-filling of different types of λ_n -AFM.** For the mean-field calculation with $\phi = 0.1, L = 30$, the ground state energy of the λ_8 -AFM mean-field Hamiltonian is lower than that of other types of Hamiltonians.

Next, we calculate the mean-field ground-state energy for different λ_n -AFM orders. From Fig. S8, we find that

λ_8 -AFM mean-field states have lower ground-state energy than other types of antiferromagnetic orders in the whole interaction regime of the ordered phases. Thus, from a mean-field perspective, the system favors the λ_8 -AFM order.

C. Phase boundary and critical exponents

Here, we perform QMC simulation through short-time relaxation to systematically study the phase boundary and critical properties of the quantum phase transition. To determine the phase boundary of the SU(3) Hubbard model with staggered flux, we compute the structure factor and correlation length ratio. For the λ_8 -AFM order, the structure factor is defined as:

$$S_{\lambda_8\text{-AFM}}(\mathbf{k}) = \frac{1}{L^{2d}} \sum_{i,j} e^{i\mathbf{k}\cdot(\mathbf{r}_i - \mathbf{r}_j)} (-1)^{i+j} \langle \mathbf{c}_i^\dagger \lambda_8 \mathbf{c}_i \mathbf{c}_j^\dagger \lambda_8 \mathbf{c}_j \rangle, \quad (\text{S28})$$

The associated correlation length ratio is defined as

$$R_{\lambda_8\text{-AFM}} \equiv 1 - \frac{S_{\lambda_8\text{-AFM}}(\mathbf{k} = \Delta\mathbf{k})}{S_{\lambda_8\text{-AFM}}(\mathbf{k} = 0)}. \quad (\text{S29})$$

The fermion correlation $G_f(\mathbf{k})$ is defined the same as Eq. (S18):

$$G_f(\mathbf{k}) \equiv \frac{1}{L^2} \sum_{ij} e^{i\mathbf{k}\cdot(\mathbf{r}_i - \mathbf{r}_j)} \langle c_{i,A}^\dagger c_{j,B} \rangle, \quad (\text{S30})$$

where A, B represent two inequivalent sublattices in a square lattice with staggered flux. In the main text and data figures, unless otherwise specified, we omit the momentum variables and denote $S_{\lambda_8\text{-AFM}} \equiv S_{\lambda_8\text{-AFM}}(\mathbf{k} = 0)$ and $G_f \equiv G_f(\mathbf{k} = \mathbf{K} + \Delta\mathbf{k})$, where $\mathbf{K} = (\pm\frac{\pi}{2}, \pm\frac{\pi}{2})$ represents the momentum at the Dirac points.

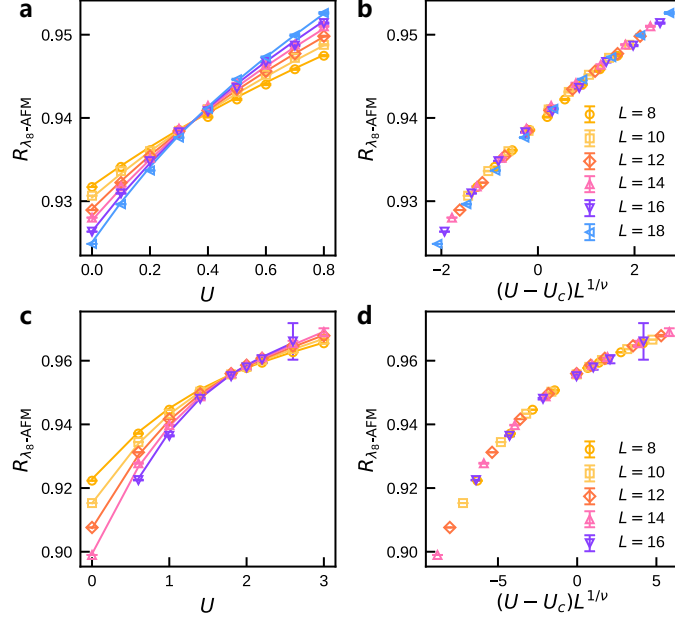


FIG. S9. Curves of $R_{\lambda_8\text{-AFM}}$ versus U for different sizes with λ_8 -AFM initial state at $\tau = 0.25L^z$. **a-b**, For $\phi = 0.05\pi$, the fitted critical point is $U_c = 0.347(4)$, with the critical exponent $1/\nu = 0.67(1)$. **c-d**, For $\phi = 0.1\pi$, the fitted critical point is $U_c = 2.0(3)$, with $1/\nu = 0.58(7)$.

To identify phase boundary between the DSM phase and the λ_8 -AFM phase, we prepare a λ_8 -AFM initial state and calculate the critical point for fixed ϕ by the method of short-time dynamics. For fixed $\tau L^{-z} = 0.25$. We calculate the critical point for $\phi = 0.05\pi$, $\phi = 0.075\pi$ and 0.1π by the intersection points of curves of $R_{\lambda_8\text{-AFM}}$ versus U for different L . As shown in Fig. S9, critical points are $U_c = 0.347(4)$ for $\phi = 0.05\pi$, $U_c = 2.0(3)$ for $\phi = 0.1\pi$, and $U_c = 1.10(5)$ for $\phi = 0.075\pi$ as shown in the main text.

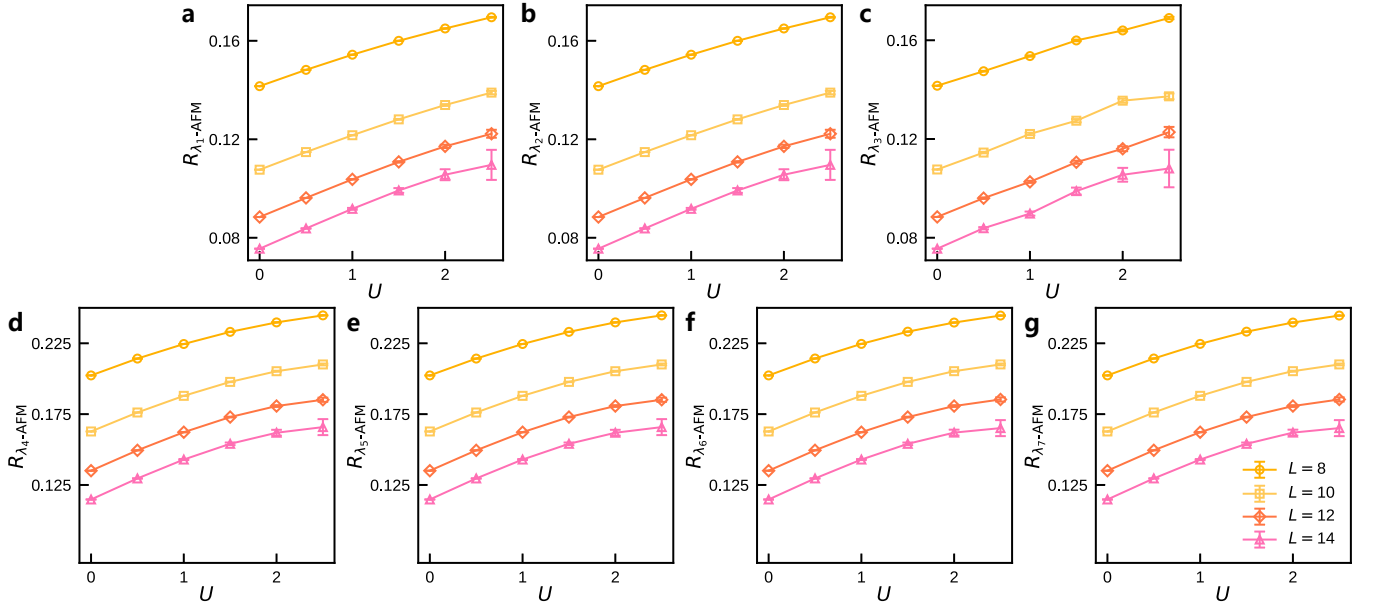


FIG. S10. Correlation-length ratios for λ_1 -AFM to λ_7 -AFM versus U for different sizes with λ_8 -AFM initial state at $\tau = 0.25L^z, \phi = 0.075\pi$. There is no crossing point in the curves of $R_{\lambda_n\text{-AFM}}$ versus U .

Here, to further confirm the λ_8 -AFM is the dominant ordering, we also compute the correlation length ratio for other quantities. We find that there is no crossing in the curves of $R_{\lambda_n\text{-AFM}}$ for the AFM orders defined by λ_1 to λ_7 versus U , as shown in Fig. S10. The results of the correlation length ratio decrease with L , demonstrating the absence of long-range order. Hence, the λ_8 -AFM is the dominant ordering, and other AFM orders are all short-range in the half-filled SU(3) Hubbard model with staggered flux.

Moreover, scaling collapse for the curves of $R_{\lambda_8\text{-AFM}}$ versus rescaled $(U - U_c)$ gives the value of $1/\nu$. Accordingly, we obtain $1/\nu = 0.67(1)$ and $1/\nu = 0.58(7)$ for $\phi = 0.05\pi$ and $\phi = 0.1\pi$, respectively. Combining $1/\nu = 0.68(5)$ with $\phi = 0.075\pi$ shown in the main text, we find that the values of $1/\nu$ are consistent with each other within error bar, showing the universality of the quantum phase transition between DSM and λ_8 -AFM ordered phase.

To determine the anomalous dimensions η_ϕ and η_ψ of the bosonic field and the fermionic field we study the relaxation dynamics of the structure factor $S_{\lambda_8\text{-AFM}} = S_{\lambda_8\text{-AFM}}(\mathbf{k} = 0)$ and the fermion correlation $G_f = G_f(\mathbf{k} = \mathbf{K} + \Delta\mathbf{k})$ at the critical point. The curves before and after rescaling are shown in Figs. S11 and S12 and Fig. 3 in the main text for different ϕ . The critical exponents determined above are summarized in Table S3, from which we find that the anomalous dimensions for different ϕ are consistent with each other within error bar, further confirming the universality of the phase transition.

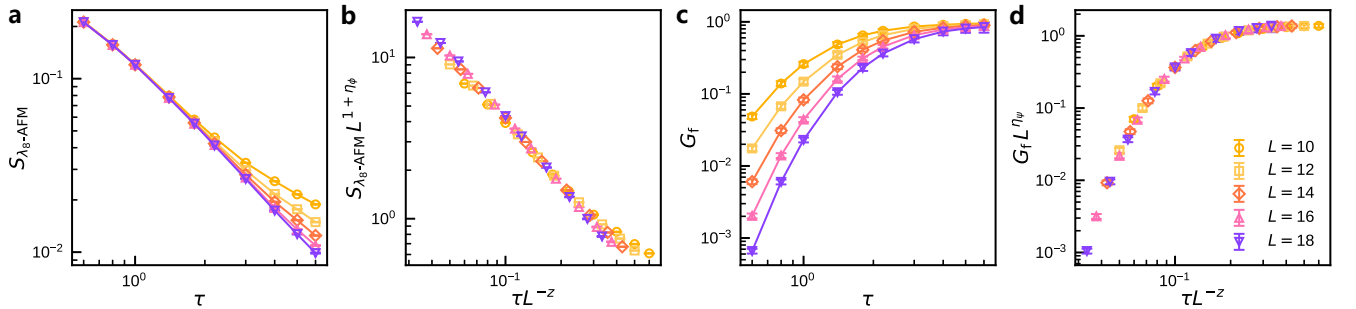


FIG. S11. Relaxation dynamics at the QCP $\phi = 0.05\pi, U = 0.347(4)$ with λ_8 -AFM initial state in SU(3) Hubbard model. **a-b**, Curves of S versus τ for different sizes before and after rescaling. **c-d**, Curves of G versus τ before and after rescaling. Data collapse in the relaxation dynamics shows $\eta_\phi = 0.51(3)$ and $\eta_\psi = 0.16(2)$.

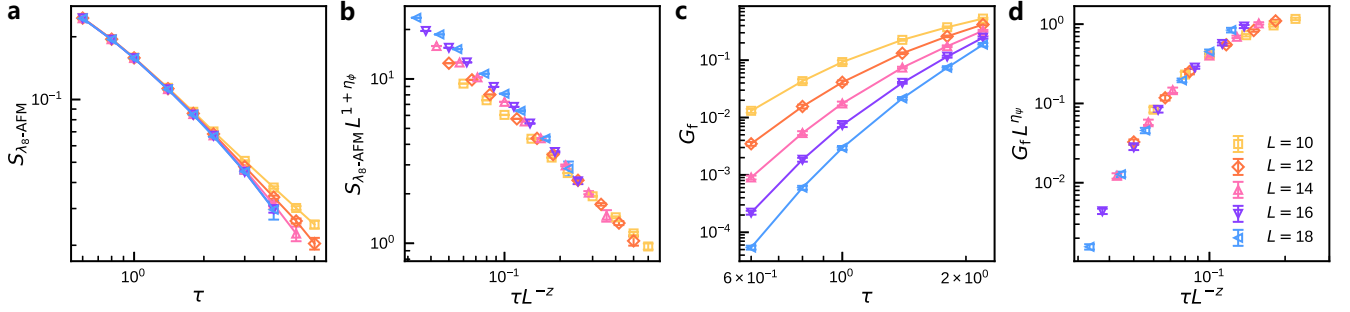


FIG. S12. **Relaxation dynamics at the QCP** $\phi = 0.1\pi, U = 2.0(3)$ with λ_8 -AFM initial state in SU(3) Hubbard model. **a-b**, Curves of S versus τ for different sizes before and after rescaling. **c-d**, Curves of G versus τ before and after rescaling. Data collapse in the relaxation dynamics shows $\eta_\phi = 0.58(10)$ and $\eta_\psi = 0.16(3)$.

TABLE S3. **Critical properties for the SU(3) Hubbard model probed under different staggered flux ϕ .**

ϕ	U_c	ν^{-1}	η_ϕ	η_ψ
0.05π	0.347(4)	0.67(1)	0.51(3)	0.16(2)
0.075π	1.10(5)	0.68(5)	0.55(5)	0.15(3)
0.1π	2.0(3)	0.58(7)	0.58(10)	0.16(3)

D. The new universality class

Our numerical results demonstrate the presence of a continuous phase transition which does not belong to any of known universality classes [71, 72]. Instead, it represents a new universality class.

In the saturated λ_8 -AFM phase, two flavors of fermions (referred to as flavors 1 and 2) are localized in one sublattice (designated as the A lattice), while the remaining flavor of fermions (referred to as flavor 3) is localized in the other sublattice (designated as the B lattice), as illustrated in Fig. 3a of the main text. It is evident that the Z_2 symmetry between the AB sublattices is significantly broken. The diagonal λ_8 generator induces a global U(1) transformation, while the generators $\lambda_1, \lambda_2, \lambda_3$ act solely on the subspace of flavors 1 and 2, generating a closed SU(2) transformation that only mixes these two flavors. Since these four generators all commute with the order parameter operator, the $SU(2) \times U(1)$ is the largest symmetry group that remains invariant under the λ_8 -AFM order parameter m after spontaneous symmetry breaking. The other four generators of the SU(3) group, $\lambda_4, \lambda_5, \lambda_6, \lambda_7$, produce transformations that alter the direction of the AFM order parameter $\{m_n\}$ in a compact manifold, leading to other λ_8 -AFM degenerate ground states, which are four independent Goldstone modes. All degenerate ground states span a 4-dimensional ground state degeneracy space, and these states can be mapped one-to-one onto points on the manifold $[SU(3) \times Z_2] / [SU(2) \times U(1)]$ [73, 74].

The critical exponents determined via the short-time dynamics in our work are summarized in Table S4 and compared with those of other Gross-Neveu universality classes with the same fermion components. It is clear that the new universality class we have discovered is distinct from the previously known classes.

TABLE S4. **Comparison of critical exponents for different Gross-Neveu-Yukawa universality classes in $d = 2 + 1$ with $N_f = 6$.** The first row, chiral $[SU(3) \times Z_2] / [SU(2) \times U(1)]$ denotes the universality class for SU(3) Dirac fermion Hubbard model, with exponents determined from nonequilibrium PQMC.

Universality class	ν^{-1}	η_ϕ	η_ψ
chiral $[SU(3) \times Z_2] / [SU(2) \times U(1)]$ (this work)	0.68(5)	0.55(5)	0.15(3)
chiral Heisenberg ($4 - \epsilon$, 2nd order)[69]	1.478	1.023	0.058
chiral XY ($4 - \epsilon$, 2nd order)[69]	1.809	0.698	0.082
chiral Ising ($4 - \epsilon$, 2nd order)[69]	0.750	0.865	0.011
chiral Ising (FRG)[70]	0.993	0.912	0.013

E. Sign problem behaviors and computational efficiency

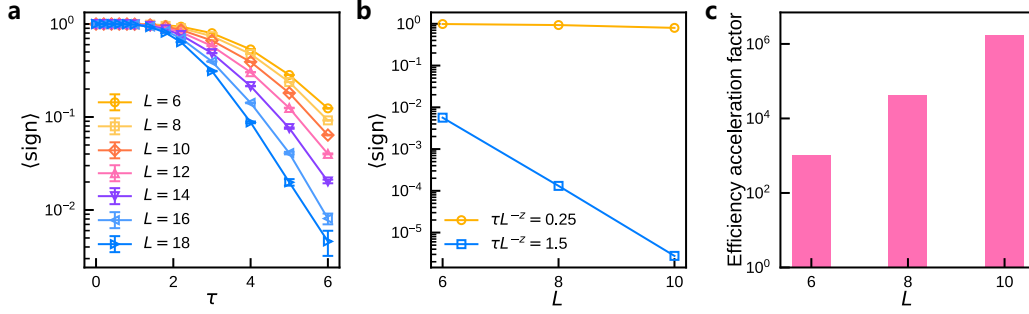


FIG. S13. **The sign problem in SU(3) Hubbard model at the QCP $\phi = 0.1, U = 2.0(3)$.** **a**, The average sign with different L and τ in short-time stage. **b**, Comparison for the average sign between short-time stage ($\tau = 0.25L^z$) and equilibrium stage ($\tau = 1.5L^z$). **c**, Efficiency gain of QMC with the short-time method ($\tau = 0.25L^z$) compared to equilibrium QMC ($\tau = 1.5L^z$) for different sizes L .

For this model, we set the parameters at the critical point $U = 2.0(3)$, $\phi = 0.1\pi$. The average sign as a function of imaginary time τ and size L is shown in Fig. S13a. The sign problem for this model is significantly more severe than for the previous two models. For $\tau = 0.25L^z$, the average sign is approximately $10^{-1} \sim 10^{-2}$, meaning that compared to the sign-problem-free case, 10 to 100 times more computational resources are needed to obtain reliable results. From Figs. S11 and S12 and Fig. 3 in the main text, it can be seen that $\tau = 0.25L^z$ is in the nonequilibrium scaling region controlled by the critical point. Even though the ground state is not reached, its nonequilibrium scaling still reflects the quantum criticality of the ground state. In equilibrium QMC studies, it is typically necessary to set the imaginary time τ to more than 1.5 times the size L^z to reach the ground state. However, evolving for such a long time, the average sign decays to approximately $10^{-5} \sim 10^{-6}$. In Fig. S13b, we compare the average sign for $\tau = 0.25L^z$ and $\tau = 1.5L^z$. Since the computational error (according to Eq. S8) is inversely proportional to the average sign $\langle \text{sign} \rangle$ (according to Eq. S8), we can measure the difference in computational efficiency by multiplying the ratio of the average sign $\langle \text{sign} \rangle$ by the length of imaginary-time evolution, as follows:

$$\text{Efficiency acceleration factor} = \frac{1/\langle \text{sign} \rangle_{\text{eq.}}}{1/\langle \text{sign} \rangle_{\text{neq.}}} \times \frac{\tau_{\text{eq.}}}{\tau_{\text{neq.}}}, \quad (\text{S31})$$

where the nonequilibrium evolution time is $\tau_{\text{neq.}} = 0.25L^z$, and the equilibrium evolution time is $\tau_{\text{eq.}} = 1.5L^z$. $\langle \text{sign} \rangle_{\text{neq.}}$ and $\langle \text{sign} \rangle_{\text{eq.}}$ are their corresponding average signs, as shown in Fig. S13b. We specifically compared the differences in computational efficiency for several system sizes, as shown in Fig. S13c. The computational resources required by the nonequilibrium method are only a few millionths of those required by the equilibrium method, and this efficiency improvement roughly grows exponentially with the system size. Consequently, our nonequilibrium method enables the QMC simulation on SU(3) Hubbard model with large system size, which is not accessible in previous unbiased numerical approaches.